



# City Research Online

## City St George's, University of London

**Citation:** Liu, F., Zhao, B., Wu, W., Yang, H., Ning, Y., Lai, Y. & Bradley, R. (2018). Low Cost, Robust, Environmentally Friendly Geopolymer–Mesoporous Carbon Composites for Efficient Solar Powered Steam Generation. *Advanced Functional Materials*, 28(47), pp. 1-11. doi: 10.1002/adfm.201803266

This is the accepted version of the paper.

This version of the publication may differ from the final published version. To cite this item please consult the publisher's version.

**Permanent repository link:** <https://openaccess.city.ac.uk/id/eprint/21118/>

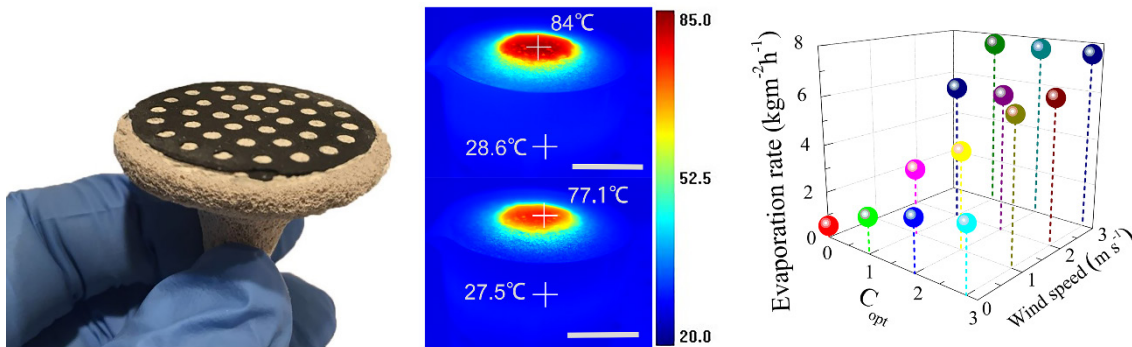
**Link to published version:** <https://doi.org/10.1002/adfm.201803266>

**Copyright and Reuse:** Copyright and Moral Rights remain with the author(s) and/or copyright holders. Copies of full items can be used for personal research or study, educational, or not-for-profit purposes without prior permission or charge, unless otherwise indicated, provided that the authors, title and full bibliographic details are credited, a hyperlink and/or URL is given for the original metadata page and the content is not changed in any way. For full details of reuse please refer to [City Research Online policy](#).

## A short summary and the Imagine of Table of Contents

### Low Cost, Robust, Environmentally Friendly Geopolymer-Mesoporous Carbon Composites for Efficient Solar Powered Steam Generation

*Fenghua Liu, Binyuan Zhao\*, Weiping Wu\*, Haiyan Yang, Yuesheng Ning, Yijian Lai and Robert Bradley*



Geopolymer-Biomass Mesoporous Carbon Composites (GBMCC) enable low cost, robust, environmentally friendly and efficient solar steam generation. A remarkable, record high water vapor generation rate up to  $7.55 \text{ kg m}^{-2} \text{ h}^{-1}$  has been achieved under 1 sun solar intensity at the wind speed of  $3 \text{ m s}^{-1}$ . This is 15 folders that of natural water evaporation rate ( $0.502 \text{ kg m}^{-2} \text{ h}^{-1}$ ).

DOI: 10.1002/(No. adfm.201803266)

**Article type: Full paper**

## **Low Cost, Robust, Environmentally Friendly Geopolymer-Mesoporous Carbon Composites for Efficient Solar Powered Steam Generation**

*Fenghua Liu, Binyuan Zhao\*, Weiping Wu\*, Haiyan Yang, Yuesheng Ning, Yijian Lai and Robert Bradley*

Dr. F. Liu, Prof. B. Zhao, Dr. H. Yang, Y. Ning, Y. Lai  
State Key Laboratory of Metal Matrix Composites,  
School of Materials Science and Engineering,  
Shanghai Jiao Tong University,  
Shanghai, 200240, China  
Email: byzhao@sjtu.edu.cn

Dr. W. Wu  
Department of Electrical and Electronic Engineering,  
School of Mathematics, Computer Science and Engineering,  
City, University of London,  
Northampton Square, London, EC1V 0HB, United Kingdom  
Email: Weiping.Wu@city.ac.uk

Prof. R. Bradley  
Department of Materials, University of Oxford,  
16 Parks Road, Oxford, OX1 3PH, United Kingdom  
MatSurf Technology Ltd.  
The Old Stables Marion Lodge, Little Salkeld, Penrith,  
Cumbria, CA10 1NW, United Kingdom

### **Corresponding Authors**

\*Email: byzhao@sjtu.edu.cn

\*Email: Weiping.Wu@city.ac.uk

### **Keywords:**

Solar Stream Generation; Ideal Solar Absorber; Porous nano Carbon Materials; Biomass Carbon and Geopolymer; Energy

## **Abstract**

High-efficiency, environment friendly, renewable energy based methods of desalination represent attractive and potentially very powerful solutions to the long-standing problem of global water shortage. Many new laboratory-scale materials have been developed for photothermal desalination but the development of low-cost, easy-to-manufacture and scalable materials and systems that can convert solar irradiation into exploitable thermal energy in this context is still a significant challenge. In this paper we present work on a Geopolymer-Biomass Mesoporous Carbon Composite (GBMCC) device with mesoporous and macroporous structures for harvesting solar energy which is then used in a device to generate water vapor with high efficiency using negative pressure, wind-driven, steam generation. The GBMCC device gives water evaporation rates of  $1.58 \text{ kg m}^{-2} \text{ h}^{-1}$  and  $2.71 \text{ kg m}^{-2} \text{ h}^{-1}$  under 1 sun and 3 suns illumination, with the solar thermal conversion efficiency up to 84.95% and 67.6%, respectively. A remarkable, record high water vapor generation rate of  $7.55 \text{ kg m}^{-2} \text{ h}^{-1}$  have been achieved under 1 sun solar intensity at the wind speed of  $3 \text{ m s}^{-1}$ . This is a key step forward today's efficient, sustainable and economical production of clean water from seawater or common wastewater with free solar energy.

The global water resource is currently under such huge pressure from rapidly growing demands, and also from climate change, that half of the 60 largest economies in the world are facing a serious risk of water shortages in the near future. Despite the development of advanced water technologies and managements, seawater desalination is known to offer the most effective long-term solution to the freshwater shortage challenge.<sup>[1]</sup> At present, reverse osmosis membrane and thermal steam evaporation are the two most widely used technologies in seawater desalination, however, they are not energy efficient or economical processes.

Very recently, solar steam generation using free, renewable solar energy, has been proposed as a new, clean and sustainable approach to address the issue of freshwater shortage. The biggest challenge for solar-driven steam generation is to develop easy-to-manufacture, large area, inexpensive materials that can convert solar irradiation into exploitable thermal energy with high efficiency and which are scalable to levels which can realistically address the problem. To that end, achieving maximum heat localisation within the thin evaporation surface, is critical in maximizing solar absorption and reducing thermal loss and so obtaining enhanced conversion efficiency.

Various novel materials have been proposed as ideal solar absorbers, such as vertically aligned single-walled carbon nanotubes,<sup>[2, 3]</sup> plasmonic metal particles,<sup>[4-8]</sup> black nano metal oxides,<sup>[9-12]</sup> and carbides<sup>[13]</sup> for localizing heat generation. Besides, the localizing heat, water transpiration have been greatly enhanced by carbon materials with tailored surface structures, such as functionalized graphene,<sup>[14-19]</sup> vertically aligned graphene sheet membranes,<sup>[20]</sup> carbon-nanotubes,<sup>[21-23]</sup> carbon-black,<sup>[24]</sup> hydrophobic hollow carbon beads,<sup>[25]</sup> and carbon composite materials.<sup>[26-29]</sup> Although most of these materials can convert solar energy to heat, most also have intrinsic limitations for water vapor generation notably such, high cost (noble metals and nano materials), environmental hazards (nano materials and some of the metal oxides), and poor mechanical properties.

Another main challenge is how to achieve optimized thermal management to enhance the efficiency<sup>[29]</sup>. In an ideal solar thermal water vapor device, the top layers and coatings function as the layer for photothermal conversion, the support materials should be hydrophilic possessing sufficient

capillarity with appropriate open porosity, so that water will be able to be freely transported to the heat localization zone rapidly and efficiently. In order to reduce the heat loss, the thermal conductivity and geometry of the support is also critical. A combination of foams with black surface for efficient sunlight absorption and thermal management have been investigated, such as AAO membranes,<sup>[30-32]</sup> gauzes,<sup>[24]</sup> papers,<sup>[33, 34]</sup> polystyrene foams,<sup>[35, 36]</sup> wood,<sup>[37-41]</sup> and macroporous silica.<sup>[42]</sup>

In order to form water paths to meet the water supply and the thermal management simultaneously, many research works have been done by compositing the two-dimensional (2D) channel paths with the insulate structures, examples include cotton rod,<sup>[43]</sup> fabric wick,<sup>[44]</sup> mushroom stipe<sup>[45]</sup> and bacterial nanocellulose.<sup>[46]</sup> Unfortunately, the optical absorption properties of these materials, are not sufficient to generate steam fast enough.

Because of these challenges and difficulties, optimized or ideal combinations of materials leading to workable systems have not yet been achieved. Scale up into large devices is also significantly hindered by cost and also the complexity of the synthesis processes. Photothermal materials with inherent relatively low chemical and mechanical stability have difficulties to scale up and be recycled/degraded in various nature environment. Therefore, it still remains a huge challenge to develop low cost, high performance, robust, scalable, and environmental friendly materials for solar steam generation.

Herein, we introduce and demonstrate a new class of geopolymer-biomass mesoporous carbon composite materials, and a new structure design for high efficiency water steam generation. Two sustainable porous materials, are synthesized completely with raw materials containing environmental compatible chemical elements, which are also known as rock-forming minerals of geological origin. The geopolymeric materials used as the support part have ultralow thermal conductivity  $0.15-0.48 \text{ W m}^{-1} \text{ K}^{-1}$  that contributes to the ideal thermal management.<sup>[47]</sup> The biomass mesoporous carbon (BMC) derived from plant biowaste, has high surface areas up to  $467 \text{ m}^2 \text{ g}^{-1}$ , enabling highly efficient solar absorption and water transportation through pores during solar steam generation process. The design is inspired by the water transpiration behavior in plants where water

is transported from the soil and released to the atmosphere through the leaves. The water transport rate highly depends on the differential pressure and diffusion resistance. Based on this principle and the two novel materials, we introduce a robust, low-cost and environmental friendly composite materials, the Geopolymer-Biomass Mesoporous Carbon Composites (GBMCC), and our novel solar steam-generation device.

The bioinspired geometry of the device as shown in **Figure 1a**, includes an umbrella-shaped disk, with a fibrous stipe with a small cross section. The significant advantage is that the mechanical strength is high enough for practical installations in any natural environment. Since all the materials and devices can be formed by press molding (see the experimental section), the mechanical strength is high enough to apply them in practical fields steadily to couple with solar and wind energy at large scale. The physical pictures, and the schematic of the heat transportation behavior of the device, are showed in Figure 1a and 1b, respectively. The integrated structures successively consist of the BMC layer, geopolymer part, and polystyrene foam. The GBMCC device was placed on the top of sea water. Water can be quickly transported from the bottom to the BMC layer by capillary action through geopolymer. When the water reached the top BMC layer which have absorbed enough solar energy, the heat located in the thin layer can help the evaporation to be activated instantly. Besides, the wind can accelerate the water vapor generation due to the reduced pressure, this effect also can be found in plants where the negative water vapor pressure greatly promotes the transpiration. Both the geometry and dimension of the devices were optimized to minimize all the three paths of heat loss, heat conduction, heat convection, and heat radiation. The ability of water vapor generation under ambient or concentrated sunlight proved the successful design of the materials and structures. Also, it can be expected to achieve significant cost reduction of existing solar thermal systems. Due to the controllability of the shape and structure of GBMCC, it is relatively easy to meet the requirements for heat transfer, heat dissipation, and water conduction.

The BMC layer was made from corn straw and the details are included in Supplementary (Section 1). The obtained BMC materials have excellent mechanical properties (compressive strength:

35 MPa, bending strength: 14 Mpa, the testing curves are showed in Supplementary, Figure S1),<sup>[48]</sup> proper pore size (3 nm to 5 nm), relatively low thermal conductivity ( $0.43 \text{ W m}^{-1} \text{ K}^{-1}$ ), ideal broadband solar absorption which lead to excellent photothermal conversion capabilities. In addition, the thin and porous BMC layer contributes to vapor escape and heat localization. The geopolymer, an environment protection material, consists of  $\text{AlO}_6$  octahedral and  $\text{SiO}_4$  tetrahedral units that allow to form three-dimensional (3D) structures easily.<sup>[49]</sup> With excellent hydrophily and proper pore structures, the geopolymer can transport bulk water rapidly from bottom to the top BMC layer where the heat localized zone locates. The polystyrene (PS) foam, a good thermal insulator (thermal conductivity  $0.034\text{-}0.04 \text{ W m}^{-1} \text{ K}^{-1}$ )<sup>[33]</sup>, encompassing the GBMCC serves as an effective thermal barrier to alleviate thermal losses to the bulk water. It can also be used to float the whole device, resulting in efficient solar steam generation right at the water-air interface.

Due to the bulk structures and the use of dust free and non-toxic materials, the devices show excellent durability and stability including high resistance to chloride, acid, thermal, freeze-thaw and efflorescence. They are safe to handle during production, shipping, installations and water evaporation operation (more discussion in the Supplementary Section 3). The cost of the device is very low, as our carbon materials cost only about \$0.0147 per gram, much cheaper than the graphene oxide GO (\$26.5 per gram),  $\text{Ti}_2\text{O}_3$  (\$4.65 per gram) or other nano materials (Supplementary Section 3). The cost of one GBMCC device (3.62 g Geopolymer, 1.8 g BMC) is only \$0.0273. The estimated large area GBMCC devices cost \$39 per square meter only ( $\$39/\text{m}^2$ ). More importantly, with the robust device, we introduced wind to the system, enabling to capture extra energy from wind, another most important source of renewable energy besides the solar radiation. With the help of wind, the evaporation rate can be greatly enhanced.

The preparation processes of the GBMCC device are showed in Figure 1c, the details are described in experimental section. Briefly, geopolymer powder was blended with DI water, then stirred at the speed of 2000 rpm for 2 min. After that, a certain amount of hydrogen peroxide (30 wt%) was added, the mixture was stirred at the same speed for another 20 s. The prepared geopolymer slurry was

transferred into a mold, and then dried in an oven at 60 °C for 24 h to form the geopolymer sample. Also, the BMC can be adhered to the geopolymer block with the same slurry to get the GBMCC.

The structures and morphologies of the BMC, the geopolymer and the interface were carefully examined by scanning electron microscopy (SEM). The interface between the geopolymer and BMC (**Figure 2a**), is the boundary and direct connections created during the two simple forming processes. From the SEM image, two materials with different colors can be found obviously, the upper layer is the BMC, the lower part is the geopolymer. With the closely connected interface between the BMC and geopolymer, as shown distinctly in the middle of the photo, the structure of GBMCC can effectively transport water from the bottom upward to the contiguous porous BMC layer, forming continuous bottom-up water transport pathways.

The porous structures of a geopolymer have larger pores, whose microstructure is shown in Figure 2b, consisting of 10-20  $\mu\text{m}$  intercommunicating pores (Supplementary Figure S2). The macroporous structure provides ideal channels for supplying water because of capillary force. The mesoporous structures with intercommunicating mesh-like channels spread all over the BMC layer were clearly observed, shown in Figure 2c and 2d. These channels provide excellent paths for efficient vapor escape. The surface area of BMC is  $467 \text{ m}^2 \text{ g}^{-1}$ , the average pore size is about 4 nm (Supplementary Figure S3), conforming the evaporation layer possesses the high surface area and mesoporous structures. The TEM images in Figure 2e and 2f clearly show that the BMC has mesoporous structures. The BMCs consist of interconnected pores with diameters around 3 nm to 5 nm, which is consistent with the pore parameters calculated using the Barrett-Joyner-Halenda (BJH) method (Figure S3).<sup>[50]</sup>

The optical absorption of the BMC coated on the geopolymer was carefully measured with an Ultraviolet-Visible-Near-Infrared (UV-Vis NIR) spectrophotometer equipped with an integrating sphere. As shown in **Figure 3a**, the GBMCC has high (90-95%) light absorption over a broad solar spectrum (250 nm-2500 nm), while a geopolymer has relative low ( $\approx 25\text{-}40\%$  within 500 nm-1800 nm) absorption of solar energy. We also compared the optical properties of dry and wet GBMCC layers. The dry GBMCC has an absorption of about 89% ranges from 250 nm to 1300 nm, and then

decrease when wavelength increases from 1300 nm to 2500 nm. Two main reasons can explain the wavelength dependent of the NIR optical absorption. Firstly, carbon materials with dominating  $sp^2$  bonds, the real ( $\epsilon'$ ) and imaginary ( $\epsilon''$ ) parts of the complex effective are determined by free carriers at IR wavelengths. Secondly, for long wavelength IR light, the depth of penetration of incident light decreases leading to a decrease in absorption and increase in reflectance. The near infrared reflectivity depends on the relative refractive index of the BMC surface and that of its surrounding medium and wavelength of the incident light. More difference between the refractive indices BMC and air-voids in porous structure also caused the reflectance increasing.<sup>[51]</sup> Therefore, the improved optical absorption has been observed in the wet GBMCC sample. The impact of the wavelength dependent absorption on the solar steam generation is low. Of the light that reaches Earth's surface, infrared radiation makes up 49.4% of while visible light provides 42.3%. The heat-producing region of the infrared radiations from the sun is from 700 nm to 1100 nm,<sup>[52]</sup> which falls into the high absorption wavelength region of our materials, so the energy loss of our device is small.

The surface chemical compositions and functional groups of BMCs were identified by X-ray Photoelectron Spectroscopy (XPS) and Fourier Transform Infrared Spectroscopy (FTIR). Figure 3b displays the XPS spectra of BMC and geopolimer. Strong C 1s (284.72 eV) and O 1s (532.22 eV) peaks were observed, as it can be expected from biomass driven carbon materials. The surface chemical element composition also can be derived from the XPS results, the amount of Carbon (C) is about 85.02%, Oxygen (O) is about 11%. In addition, the N 1s (401.02 eV) signal was also detected in BMC layer with a weak peak corresponding to C-N/N-H, and the concentration of Nitrogen (N) atoms is about 1.72%. The nitrogen element is from the biomass, as the C-N/N-H chemical structures have been formed during high temperature process when synthesis the materials. Meanwhile, the peaks in FTIR spectra (Figure 3c) for BMC are observed at  $3419\text{ cm}^{-1}$  and  $1109\text{ cm}^{-1}$ ,  $1402.9\text{ cm}^{-1}$  and  $1631\text{ cm}^{-1}$  further confirm the existence of C-N/N-H chemical structures in the materials. While for the geopolimer, the existent of -OH and Si-O-Si, Al-O-Si are confirmed by the XPS data. The

oxygen-containing functional groups can contribute to the hydrophilic properties for the BMC and geopolymer.

The functional groups make the surface be highly hydrophilic, which is highly beneficial for efficient solar steam generation. The hydrophilic nature of both geopolymer and BMC enables very efficient water supply when the GBMCC is floating on the surface of water. We monitored the process of fast water capillarity effect using real-time wetting process images captured by an infrared (IR) camera (Figure 3d). To obtain adequate contrast in the IR images, the experiment had been carried out without illumination using a water bath with slightly higher temperature (30 °C) than the GBMCC device at the room temperature (25 °C). Once GBMCC came in contact with water, the whole piece of GBMCC could be entirely filled with water within 30 seconds. It indicates that the highly hydrophilic GBMCC can pump water rapidly from bottom up to the evaporation area (Supplementary Video S1), and it is the prerequisite for efficient solar steam generation.

Another key factor to control the heat effectively located in the evaporation layer not transferred to the bulk water and the environment is the shape of the device. As mentioned previously, the geometry of GBMCC can be easily optimized for minimizing the heat loss including conduction, convection, and radiation (Figure 1a). The rough surface of the top BMC with a large surface-projected area ratio enables stronger evaporation and also consequently convection and radiation losses are expected to be suppressed. The geometry of geopolymer was machined to various shapes, such as pie, cylinder and cone, and finally the slender stipe can satisfy both the water supply and smallest contact area to environment which can reduce the heat loss maximally. We machined the geopolymer part to be slender stipe immersed into bulk water, the size was designed to match with the water supply. With this structure, the majority of the generated heat will not be transferred to the bulk water. The thickness of the BMC also should be kept in proper range, because too thick BMC can reduce the evaporation rate due to increased path for water vapor. If the BMC layer is too thin, the solar thermal absorption will be reduced because of increasing reflectivity and transmissivity, moreover, the mechanical strength of thin BMC layer will not be high enough.

The thermal conductivity of the geopolymer is also a critical factor in the water evaporation. The thermal conductivity of geopolymer is  $0.261 \text{ W m}^{-1} \text{ K}^{-1}$  (the details of the calculation are shown in Supplementary Section 7), is significantly lower than water ( $0.60 \text{ W m}^{-1} \text{ K}^{-1}$ ). The lower thermal conductivity of the geopolymer, the better the heat will be localized. It is not necessary for the solar absorber layer to have the lowest thermal conductivity. However, for thin absorber, it may need the low thermal conductivity. If the absorber has a non-negligible thickness, it then requires a good heat transfer ability to absorb more energy and provide more heating sites to generate water vapor.

With the rough and proper thick BMC as the absorber, the optimized geometrical shape (slender stripe) of the geopolymer as the water transport channels, together with the polystyrene foam as the thermal insulation layer, the majority of the generated heat will be localized mainly on the surface of the BMC layer, but not be transferred to the bulk water, therefore an ideal thermal management system thus can be realized. Thus, the local temperature will increase rapidly upon solar irradiation, inducing water to evaporate faster to the atmosphere. The mechanism of the water up flow is very similar to water transpiration effect in plants. The negative pressure at the top of the BMC due to water evaporation can induce very large capillary force inside the GBMCC channels. The low thermal conductivity, proper geometrical and macro pore size are reasonable of the geopolymer to realize the heat management in respect of the water supply amount which equal the water vapor generation. Proper thickness and thermal conductivity are also beneficial for the BMC to localize enough energy to heat the water.

To systematically evaluate the performance of the GBMCC solar steam devices, the evaporation rates and energy conversion efficiencies were experimentally measured under different solar illumination conditions. The whole steam generator setup includes a precision balance and exposed to a solar simulator with an illumination intensity from  $1 \text{ kW m}^{-2}$  (1 sun) up to  $3 \text{ kW m}^{-2}$  (3 suns). The water evaporation rates are measured by recording the mass change as a function of time under the solar intensities of 1, 2 and 3 suns. Each experiment lasts for more than 60 minutes.

**Figure 4a** shows the typical solar thermal evaporation curves of time-dependent mass change under various solar illumination conditions. The evaporation rates were calculated from the slope of the curves. The evaporation rates for GBMCC is measured to be  $1.58 \text{ kg m}^{-2} \text{ h}^{-1}$  at 1 sun solar intensity, while it is  $0.502 \text{ kg m}^{-2} \text{ h}^{-1}$  for blank water surface. As the solar illumination intensity increases, the evaporation rates increase remarkable, it reached almost 1.5 times to be  $2.24 \text{ kg m}^{-2} \text{ h}^{-1}$  at 2 suns, and further increased to  $2.71 \text{ kg m}^{-2} \text{ h}^{-1}$  at 3 suns solar intensities. The incensement can be well explained by the fact that at the molecular level, the evaporation happens until the hydrogen bonds broke at the interface.<sup>[53]</sup> The higher solar energy absorbed by the evaporation layer, the higher evaporation rate will be.

**Table 1.** Solar steam generation performances of different materials. The solar absorption, the energy conversion efficiency and the evaporation rates of various photothermal materials under 1 sun.

Sample	Solar absorption [%]	Energy conversion [%]	Evaporation rate [ $\text{kg m}^{-2} \text{ h}^{-1}$ ]	References
Vertically Aligned CNT Arrays	99	30	---	[2]
CNT-coated wood membrane	98	65	0.95	[3]
Plasmonic Ag particles	---	82.45	1.008 ( $16.8 \text{ g m}^{-2} \text{ min}^{-1}$ )	[6]
Black $\text{TiO}_x$ particles	91.3	50.30	0.8012	[8]
$\text{Ti}_2\text{O}_3$ Nanoparticles	92.5	$92.1 \pm 3.2$	1.32	[12]
MXene $\text{Ti}_3\text{C}_2$	---	84	1.33 (2 kg/90 min)	[13]
Functionalized-rGO	---	48	0.47	[14]
rGO/MCE	---	60	0.838	[15]
Porous N-doped graphene	---	80	1.5	[16]
CNT nanofluid	---	---	1.1	[21]
Carbon beads	---	---	1.28	[24]
Graphene oxide-based aerogels	92	86.5	1.622	[25]
Flamed-treated wood	---	72	1.05	[39]
CNT-macroporous silica	---	82	1.31	[42]
Carbonized Mushroom	---	78	1.475	[45]
Hierarchical graphene foam	85-95	91.4	1.4	[54]
CNT modified filter paper	---	75	1.15	[55]
Hierarchically nanostructured gel	>95	94	3.2	[56]
Nitrogen enriched carbon sponge	>95	85	1.31	[57]
GBMCC without wind	90-95	84.95	1.58	This work
GBMCC with 1, 2 and 3 $\text{m s}^{-1}$ wind	90-95	---	2.85, 5.90 and 7.55	This work

The GBMCC device with robust structure can easily get excellent and outstanding performances compare to devices with other new materials in evaporation and energy conversion (**Table 1**). The energy efficiency (84.95%) is comparable to the record value reported in the field. In addition, our materials, structures and fabrication processes are robust, inexpensive and environmentally friendly compared to the counterparts. On top of these characteristics, the enhanced evaporation rate can be easily reached by coupling with wind, which will be discussed below.

To investigate solar thermal evaporation behaviour in GBMCC device under 1 sun and 3 suns intensity, an infrared camera was used to mapping the temperature field. The average temperature ( $T_{av}$ ) on the top of BMC layer are plotted in Figure 4b as a function of illumination time. When the light was turned on, a rapid temperature increase in  $T_{av}$  was observed. The temperature of GBMCC reached the equilibrium state within a short time, indicating a strong solar absorption by the material. According to the temperature-time curves,  $t \approx 400$  s and  $t \approx 810$  s are needed under 1 sun and 3 suns to obtain quasi-steady states. As expected, after 1 h illumination,  $T_{av}$  of the surface in GBMCC under 1 sun and 3 suns reached 42.2 °C and 82.1 °C, respectively. According to the Planck's law of black-body radiation, the radiation can be calculated by <sup>[58]</sup>,

$$u_{planck}(\nu) = \frac{8\pi h\nu^3}{c^2} \frac{1}{e^{h\nu/kT} - 1} \quad (1)$$

where  $u_{planck}(\nu)$  is the spectral radiance (the power per unit solid angle and per unit of area normal to the propagation) density of frequency,  $h$  is the Planck constant,  $c$  is the speed of light in a vacuum,  $k$  is the Boltzmann constant,  $\nu$  is the frequency of the electromagnetic radiation, and  $T$  is the absolute temperature of the body.

As the temperature of the black body is low, the radiation energy losses of the device can be ignored. But the radiation recorded by an infrared (IR) camera, could be very useful to map the temperature distribution on the surfaces. Typical IR imagines of the surfaces were collected and illustrated in Figure 4c and 4d, which can further conform the detailed discussions above. From the

IR imagines, it is very clear that only the BMC layer possess high temperature, indicating the absorbed solar energy was localized on the BMC layer, little energy was transferred to the bulk water.

The energy conversion efficiency ( $\eta_{th}$ ) is used as a measure to evaluate the overall solar-to-vapour efficiency. It is defined in the same way as those in recent studies,<sup>[20]</sup>

$$\eta_{th} = \frac{\dot{m}h_{LV}}{C_{opt}q_i} \quad (2)$$

where  $\dot{m}$  is the mass loss rate per unit area calculated from the slop of mass loss curves at the steady state,  $h_{LV}$  is the total enthalpy of sensible heat (315 J g<sup>-1</sup>, from ca. 25 °C to 100 °C with specific heat of water 4.2 J g<sup>-1</sup> K<sup>-1</sup>) and liquid-vapor phase change (2256 J g<sup>-1</sup>),  $C_{opt}$  is the optical concentration, and  $q_i$  is the nominal direct solar irradiation of 1 kW m<sup>-2</sup>, this irradiance corresponds to Standard Testing Conditions (STC) and is called “peak sun” or “1 sun”. When calculating the evaporation rate, the background data 0.224 kg m<sup>-2</sup> h<sup>-1</sup> in dark environment will be subtracted from all the measured (Supplementary Figure S5).

In our devices and structures, the efficiencies were calculated to be 84.95%, 82.43% and 67.6% for GBMCC at the power density of 1, 2 and 3 kW m<sup>-2</sup>, as being plotted in Figure 4e and summarised in Table 1. The pore size of the BMC fits to the evaporation under 1 sun, however, when the solar illumination increased, the speed of water vapor escaped from the device cannot match with the increased solar energy absorbed. During the water vapor generating process, the vapor pressure on the device is increased, which can hinder the water vapor getting away from the BMC. Besides, the hydrophilia and the pore size can hold the water molecule to some extent. Because of these two reasons, the efficiencies decreased when the solar power density increase. The efficiency of the GBMCC device (84.95%), has been very closed to the best samples under 1 sun reported <sup>[12, 25, 54, 56, 57]</sup>. Besides, our devices are made in a cheap, sustainable materials that are easy to manufacture and scale up. The effect of the geopolymer on water evaporation rate was also considered and tested, although this part is much lower than the GBMCC device on the water vapor generation

(Supplementary Section 9 and Table S2). Our compact devices have achieved high power per area in the range of  $1 \text{ kW m}^{-2}$  to  $2 \text{ kW m}^{-2}$ .

The cycle stability performance of the GBMCC was also conducted under 1 sun and 3 suns, as shown in Figure 4f. It is found that the performance is maintained almost unchanged for more than 10 cycles, with each cycle being over 0.5 h, demonstrating excellent stability. We attribute the stability to the inert materials used, as well as the excellent mechanical properties of GBMCC. In addition to the mechanical strength, the GBMCC materials are high stiffness-to-weight ratio, they are easy to shape, inexpensive and easy to recycle. These superior characteristics are very important for the designs and engineering towards different practical applications aiming for a variety of environmental conditions.

Photothermal devices and systems are generally installed in the fields, deserts, offshores or seas with windy conditions, to harvest solar steam. Also, the wind can accelerate the water vapor generation due to the reduced pressure. In this paper, we focused on the way of using wind to reduce the water vapor pressure. The negative pressure induced by wind can easily and greatly increase the evaporation rate. It is found that our samples show much better evaporation rates and higher efficiencies upon wind flows. A diagram between the mass change observed at different wind speed is presented in the **Figure 5a**. The evaporation rates at steady-state were calculated to be  $2.85 \text{ kg m}^{-2} \text{ h}^{-1}$ ,  $5.90 \text{ kg m}^{-2} \text{ h}^{-1}$  and  $7.55 \text{ kg m}^{-2} \text{ h}^{-1}$  under 1 sun solar intensity at the wind speed of 1, 2 and  $3 \text{ m s}^{-1}$ , respectively. These results are 1.8 to 5 folders higher than the evaporation rate without wind ( $1.58 \text{ kg m}^{-2} \text{ h}^{-1}$ ). Our evaporation rate results are about 2-5 folders of the best results reported under the same conditions, 5.7 to 15 folders that of natural water evaporation rate ( $0.502 \text{ kg m}^{-2} \text{ h}^{-1}$ ).

The corresponding results with wind under 3 suns solar intensity showed further enhancement, as being shown in Figure 5b. At the speed of wind of  $1 \text{ m s}^{-1}$ , the evaporation rate reached as high as  $5.8 \text{ kg m}^{-2} \text{ h}^{-1}$ , 2.04 times that of at 1 sun solar intensity with the same wind speed. Under this condition, when the speed of wind increases, the evaporation rate improved slightly, to  $6.41 \text{ kg m}^{-2}$

$\text{h}^{-1}$  and  $7.53 \text{ kg m}^{-2} \text{ h}^{-1}$  respectively with the wind speeds of  $2 \text{ m s}^{-1}$  and  $3 \text{ m s}^{-1}$ . The influence of sunlight intensity and wind speed on evaporation rates can be clearly seen in Figure 5c. It is found that even the low speed of wind also has a great influence on the water vapor generation, while the strong solar illumination does not have as significant effect as the high speed wind does. This indicates that the appropriate increase in wind, can significantly improve the evaporation rate. The evaporation rate changes linearly with the surface area, and convective can greatly improve the evaporation in the nano channels. The evaporation rates at high wind speed and high solar intensity both reach a maximum value at saturation, due to the finite water transport capability limited by the pore size of the BMC (3 nm), but less affected by the geopolymer as it has much large pore sizes (10-20  $\mu\text{m}$ ).

In order to understand the greatly improved steam generation rates with wind, we studied the dynamics of the process. From the infrared photos (Figure 5d), the surface temperature with  $1 \text{ m s}^{-1}$  wind is nearly  $7 \text{ }^\circ\text{C}$  lower than without wind, which is due to the extra evaporation caused by the wind flow. It took about 1100 s under sun illumination to achieve the steady-state evaporation, this is coincided well with the time for the surfaces of two samples to achieve a steady temperature (Figure 5e). This evaporation process, also strongly took energy away from the bulk water.

The cycle solar steam generation performance of the GBMCC was conducted with an intensity of 1 sun and 3 suns. The performance demonstrated excellent stability with 6 cycles. As is shown in the Figure 5f, the evaporation rate under 1 sun, with the wind speed  $1 \text{ m s}^{-1}$  is the lowest, while which under 1 sun with wind speed  $2 \text{ m s}^{-1}$  has the similar effect with under 3 suns with wind speed  $1 \text{ m s}^{-1}$ . What's more, it shows clearly that the highest evaporation rate was achieved with wind speed of  $3 \text{ m s}^{-1}$ , both under 1 sun and 3 suns.

To summarize, we developed a new concept of low cost, environmentally friendly, geopolymer-biomass mesoporous carbon photothermal composite materials for high performance solar steam generation. The materials are synthesized at low cost completely with raw materials only containing

rock-forming chemical elements that exist in geological minerals. The proper combinations of materials with optimized chemical and porous structures, perfect light absorption abilities, excellent mechanical characteristics, tailored structure and geometry, together with perfect thermal management, promise a new approach towards industrial scale, low cost and high efficient solar thermal generation technologies. Enhanced solar steam generation by wind has been discovered in these new materials for the first time. The energy conversion efficiency is as high as 84.95%, more than three time of the efficiency of silicon solar cells. A remarkable, record high water vapor generation rate of  $7.55 \text{ kg m}^{-2} \text{ h}^{-1}$  have been achieved under 1 sun solar intensity at a wind speed of  $3 \text{ m s}^{-1}$ . This result is 15 folders of the nature evaporation rate of water ( $0.502 \text{ kg m}^{-2} \text{ h}^{-1}$ ). It stands as one of the best among the state of the art solar thermal systems, and is a big step forward to clean water production from sea water or common wastewater with free solar energy.

## **Experimental Section**

*Materials and chemicals:* All chemicals and solvents in the experiments were of analytical grades and used without any further purification. Hydrogen peroxide (30 wt%), sodium chloride (NaCl) and anhydrous ethanol were purchased from Sigma-Aldrich. Deionized water was generated from a TTL-30C Ultrapure Water Generator, with electrical resistivity of  $18.2 \text{ M}\Omega \cdot \text{cm}$ . Biomass mesoporous carbon (BMC) samples were prepared from corn straw. The geopolymer powders were provided by Qufu Tembton Technology Co. Ltd., Shandong, China.

*Fabrication of GBMCC Material:* Typically, the geopolymer powder (150 g) was mixed with DI water (55 mL) in a breaker, then the mixture was stirred at the speed of 2000 rpm for 2 min. After that, hydrogen peroxide (2 mL, 30 wt%) was added in the dispersion, the mixture was stirred at the same speed for another 20 s. The prepared geopolymer slurry was transfered into a mold in a proper shape. Then the slurry (5 g) was dried in an oven at  $60 \text{ }^\circ\text{C}$  for 24 h to form the geopolymer sample. The slurry was also used to coat on the bottom surface of the BMC to bond it firmly with the

geopolymer block to get the composite GBMCC. Finally, the GBMCC and geopolymer samples were processed and polished to precise dimensions.

*Characterizations:* The microstructures of BMCs and geopolymer composites were characterized by a field-emission scanning electron microscopy (SEM, FEI Sirion 200, 5 kV). The X-ray Photoelectron Spectroscopy (XPS) analyses were carried out on Kratos AXIS Ultra DLD X-ray Photoelectron Spectrometer with a Delay Line Detector using an aluminum (Al) monochromatic X-ray source. The FTIR spectra were obtained on a Nicolet 6700 Fourier Transform Infrared (FTIR) spectrometer. The surface areas of samples were measured by a TriStar 3000 surface area analyzer (Micromeritics) by running N<sub>2</sub> adsorption Brunauer-Emmett-Teller (BET) tests. The optical spectrum of prepared samples were measured from 250 nm to 2500 nm by a UV-Vis NIR Spectrometer (PerkinElmer, Lambda 750S, USA) equipped with an integrating sphere. The absorption was then calculated by  $A=1-R-T$ , where R and T are the reflection and transmission, respectively. The infrared photographs and videos were captured by using an IR camera (MAG32, Magnity Electronics, China). The thermal diffusivity was measured by a Netzsch LFA 447 Nanoflash Thermal Diffusivity, and the specific heat capacity was measured by differential scanning calorimetry (DSC 204 F1, Phoenix).

*Solar Evaporation Tests:* A sodium chloride (3.5 wt%, NaCl) solution was prepared in a 200 mL glass beaker. A GBMCC device with a polystyrene foam was placed into the water and it floated above the water surface. The edges were carefully sealed to avoid the natural evaporation through the residual uncovered water surface between the sample and the beaker. The sunlight with a collimated beam diameter of 3 cm were provided by a Newport Oriel 94043 AAA Class Solar Simulator. The solar radiation was fixed vertically 14 cm above the GBMCC surface. A piece of Fresnel lens (26 cm×18 cm, focal length: 300 mm, OpticLens) was used to concentrate the solar light. The 1 sun intensity and 2 suns, 3 suns concentrated solar light were calibrated using an optical power meter (S310C, Thorlabs Inc). The beaker of water was placed on a computer driven analytical balance, which monitored the water mass loss in real time.

## **Supporting Information**

Supporting Information is available from the Wiley Online Library or from the author.

## **Acknowledgements**

B. Y. Z., W. P. W. and R. B. planned, supervised the project and designed the experiments. F. H. L., H. Y. Y., Y. S. N. and Y. J. L. carried out experiments, including sample fabrications, measurement and data collection. F. H. L., B. Y. Z., W. P. W. and R. B. analysed the data, drafted the manuscript. All the authors participated in the data analysis, discussion and commented on the manuscript. We thank the help provided by Professor Huiyun Liu and Tao Xu from the University College London (UCL), UK. This work is supported by the Innovate UK (Grant 104013) and the Science and Technology Department of Shanghai Municipality (STCSM) (Grant 17230732700).

Received: ((will be filled in by the editorial staff))

Revised: ((will be filled in by the editorial staff))

Published online: ((will be filled in by the editorial staff))

## References

- [1] M. A. Shannon, P. W. Bohn, M. Elimelech, J. G. Georgiadis, B. J. Marinas, A. M. Mayes, *Nature* **2008**, 452, 301.
- [2] Z. Yin, H. Wang, M. Jian, Y. Li, K. Xia, M. Zhang, C. Wang, Q. Wang, M. Ma, Q. S. Zheng, Y. Zhang, *ACS Appl. Mater. Interfaces* **2017**, 9, 28596.
- [3] C. Chen, Y. Li, J. Song, Z. Yang, Y. Kuang, E. Hitz, C. Jia, A. Gong, F. Jiang, J. Y. Zhu, B. Yang, J. Xie, L. Hu, *Adv. Mater.* **2017**, 29, 1701756
- [4] M. Gao, P. K. N. Connor, G. W. Ho, *Energy Environ. Sci.* **2016**, 9, 3151.
- [5] L. Zhou, Y. Tan, J. Wang, W. Xu, Y. Yuan, W. Cai, S. Zhu, J. Zhu, *Nat. Photonics* **2016**, 10, 393.
- [6] H. Wang, L. Miao, S. Tanemura, *Sol. RRL* **2017**, 1, 1600023.
- [7] C. Liu, J. Huang, C.-E. Hsiung, Y. Tian, J. Wang, Y. Han, A. Fratalocchi, *Adv. Sustainable Syst.* **2017**, 1, 1600013.
- [8] A. Guo, Y. Fu, G. Wang, X. Wang, *RSC Adv.* **2017**, 7, 4815.
- [9] M. Ye, J. Jia, Z. Wu, C. Qian, R. Chen, P. G. O'Brien, W. Sun, Y. Dong, G. A. Ozin, *Adv. Energy Mater.* **2017**, 7, 1601811.
- [10] D. Ding, W. Huang, C. Song, M. Yan, C. Guo, S. Liu, *Chem. Commun. (Cambridge, U. K.)* **2017**, 53, 6744.
- [11] G. Zhu, J. Xu, W. Zhao, F. Huang, *ACS Appl. Mater. Interfaces* **2016**, 8, 31716.
- [12] J. Wang, Y. Li, L. Deng, N. Wei, Y. Weng, S. Dong, D. Qi, J. Qiu, X. Chen, T. Wu, *Adv. Mater.* **2017**, 29, 1603730.
- [13] R. Li, L. Zhang, L. Shi, P. Wang, *ACS Nano* **2017**, 11, 3752.
- [14] J. Yang, Y. Pang, W. Huang, S. K. Shaw, J. Schiffbauer, M. A. Pillers, X. Mu, S. Luo, T. Zhang, Y. Huang, G. Li, S. Ptasinska, M. Lieberman, T. Luo, *ACS Nano* **2017**, 11, 5510.
- [15] G. Wang, Y. Fu, X. Ma, W. Pi, D. Liu, X. Wang, *Carbon* **2017**, 114, 117.
- [16] Y. Ito, Y. Tanabe, J. Han, T. Fujita, K. Tanigaki, M. Chen, *Adv. Mater.* **2015**, 27, 4302.

- [17] S. P. Surwade, S. N. Smirnov, I. V. Vlassioux, R. R. Unocic, G. M. Veith, S. Dai, S. M. Mahurin, *Nat. Nanotechnol.* **2015**, *10*, 459.
- [18] G. Ni, N. Miljkovic, H. Ghasemi, X. Huang, S. V. Boriskina, C.-T. Lin, J. Wang, Y. Xu, M. M. Rahman, T. Zhang, G. Chen, *Nano Energy* **2015**, *17*, 290.
- [19] L. Zhang, R. Li, B. Tang, P. Wang, *Nanoscale* **2016**, *8*, 14600.
- [20] P. Zhang, J. Li, L. Lv, Y. Zhao, L. Qu, *ACS Nano* **2017**, *11*, 5087.
- [21] X. Wang, Y. He, G. Cheng, L. Shi, X. Liu, J. Zhu, *Energy Convers. Manage.* **2016**, *130*, 176.
- [22] N. Selvakumar, S. B. Krupanidhi, H. C. Barshilia, *Adv. Mater.* **2014**, *26*, 2552.
- [23] H. Y. Yang, Z. J. Han, S. F. Yu, K. L. Pey, K. Ostrikov, R. Karnik, *Nat. Commun.* **2013**, *4*, 2220.
- [24] Y. Liu, J. Chen, D. Guo, M. Cao, L. Jiang, *ACS Appl. Mater. Interfaces* **2015**, *7*, 13645.
- [25] Y. Zeng, K. Wang, J. Yao, H. Wang, *Chem. Eng. Sci.* **2014**, *116*, 704.
- [26] X. Hu, W. Xu, L. Zhou, Y. Tan, Y. Wang, S. Zhu, J. Zhu, *Adv. Mater.* **2017**, *29*, 1604031.
- [27] H. Ghasemi, G. Ni, A. M. Marconnet, J. Loomis, S. Yerci, N. Miljkovic, G. Chen, *Nat. Commun.* **2014**, *5*, 4449.
- [28] B. Sharma, M. K. Rabinal, *J. Alloys Compd.* **2017**, *690*, 57.
- [29] L. Zhu, M. Gao, C. K. N. Peh, G. W. Ho, *Mater. Horiz.* **2018**, *5*, 323.
- [30] K. Bae, G. Kang, S. K. Cho, W. Park, K. Kim, W. J. Padilla, *Nat. Commun.* **2015**, *6*, 10103.
- [31] Y. Liu, S. Yu, R. Feng, A. Bernard, Y. Liu, Y. Zhang, H. Duan, W. Shang, P. Tao, C. Song, T. Deng, *Adv. Mater.* **2015**, *27*, 2768.
- [32] B. Fang, C. Yang, C. Pang, W. Shen, X. Zhang, Y. Zhang, W. Yuan, X. Liu, *Appl. Phys. Lett.* **2017**, *110*, 141103.
- [33] Z. Liu, H. Song, D. Ji, C. Li, A. Cheney, Y. Liu, N. Zhang, X. Zeng, B. Chen, J. Gao, Y. Li, X. Liu, D. Aga, S. Jiang, Z. Yu, Q. Gan, *Global Challenges* **2017**, *1*, 1600003.
- [34] J. Lou, Y. Liu, Z. Wang, D. Zhao, C. Song, J. Wu, N. Dasgupta, W. Zhang, D. Zhang, P. Tao, W. Shang, T. Deng, *ACS Appl. Mater. Interfaces* **2016**, *8*, 14628.

- [35] L. Shi, Y. Wang, L. Zhang, P. Wang, *J. Mater. Chem. A* **2017**, *5*, 16212.
- [36] X. Li, W. Xu, M. Tang, L. Zhou, B. Zhu, S. Zhu, J. Zhu, *Proc. Natl. Acad. Sci. U. S. A.* **2016**, *113*, 13953.
- [37] K. K. Liu, Q. Jiang, S. Tadepalli, R. Raliya, P. Biswas, R. R. Naik, S. Singamaneni, *ACS Appl. Mater. Interfaces* **2017**, *9*, 7675.
- [38] F. Chen, A. S. Gong, M. Zhu, G. Chen, S. D. Lacey, F. Jiang, Y. Li, Y. Wang, J. Dai, Y. Yao, J. Song, B. Liu, K. Fu, S. Das, L. Hu, *ACS Nano* **2017**, *11*, 4275.
- [39] G. Xue, K. Liu, Q. Chen, P. Yang, J. Li, T. Ding, J. Duan, B. Qi, J. Zhou, *ACS Appl. Mater. Interfaces* **2017**, *9*, 15052.
- [40] J. Wang, Z. Liu, X. Dong, C.-E. Hsiung, Y. Zhu, L. Liu, Y. Han, *J. Mater. Chem. A* **2017**, *5*, 6860.
- [41] X. Wu, G. Y. Chen, W. Zhang, X. Liu, H. Xu, *Adv. Sustainable Syst.* **2017**, *1*, 1700046.
- [42] Y. Wang, L. Zhang, P. Wang, *ACS Sustainable Chem. Eng.* **2016**, *4*, 1223.
- [43] X. Li, R. Lin, G. Ni, N. Xu, X. Hu, B. Zhu, G. Lv, J. Li, S. Zhu, J. Zhu, *Natl. Sci. Rev.* **2018**, *5*, 70.
- [44] G. Ni, G. Li, Svetlana V. Boriskina, H. Li, W. Yang, T. Zhang, G. Chen, *Nat. Energy* **2016**, *1*, 16126.
- [45] N. Xu, X. Hu, W. Xu, X. Li, L. Zhou, S. Zhu, J. Zhu, *Adv. Mater.* **2017**, *29*, 1606762.
- [46] Q. Jiang, L. Tian, K. K. Liu, S. Tadepalli, R. Raliya, P. Biswas, R. R. Naik, S. Singamaneni, *Adv. Mater.* **2016**, *28*, 9400.
- [47] Z. Zhang, J. L. Provis, A. Reid, H. Wang, *Cem. Concr. Compos.* **2015**, *62*, 97.
- [48] F. Wang, Y. Lai, B. Zhao, X. Hu, D. Zhang, K. Hu, *Chem. Commun. (Cambridge, U. K.)* **2010**, *46*, 3782.
- [49] Y. He, L. Liu, L. He, X. Cui, *Ceram. Int.* **2016**, *42*, 10908.
- [50] L. G. J. Elliott P. Barrett, and Paul P. Halenda, *J. Am. Chem. Soc.* **1951**, *73*, 373.

- [51] N. Kiomarsipour, R. Shoja Razavi, K. Ghani, M. Kioumarsipour, *Appl. Surf. Sci.* **2013**, *270*, 33.
- [52] G. George, V. S. Vishnu, M. L. P. Reddy, *Dyes Pigm.* **2011**, *88*, 109.
- [53] Y. Nagata, K. Usui, M. Bonn, *Phys. Rev. Lett.* **2015**, *115*, 236102.
- [54] H. Ren, M. Tang, B. Guan, K. Wang, J. Yang, F. Wang, M. Wang, J. Shan, Z. Chen, D. Wei, H. Peng, Z. Liu, *Adv. Mater.* **2017**, *29*, 1702590.
- [55] P. Yang, K. Liu, Q. Chen, J. Li, J. Duan, G. Xue, Z. Xu, W. Xie, J. Zhou, *Energy Environ. Sci.* **2017**, *10*, 1923.
- [56] F. Zhao, X. Zhou, Y. Shi, X. Qian, M. Alexander, X. Zhao, S. Mendez, R. Yang, L. Qu, G. Yu, *Nat. Nanotechnol.* **2018**, *13*, 489.
- [57] L. Zhu, M. Gao, C. K. N. Peh, X. Wang, G. W. Ho, *Adv. Energy Mater.* **2018**, *8*, 1702149.
- [58] N. N. Sharma, *J. Nanopart. Res.* **2007**, *10*, 333.

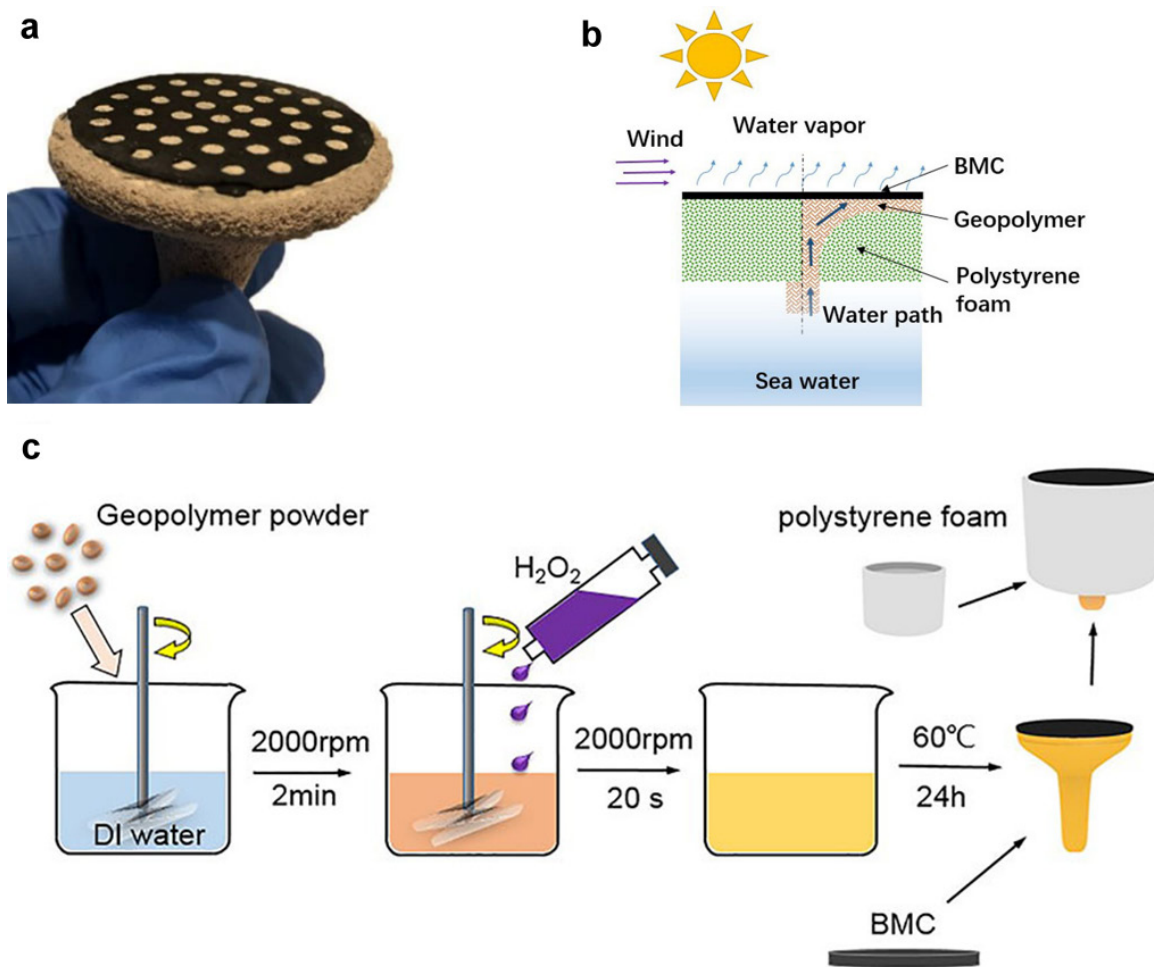


**Figure 1.** The structure and preparation of Geopolymer-Biomass Mesoporous Carbon Composite (GBMCC). a) A photo of a typical GBMCC device composing with geopolymer (brown) and biomass mesoporous carbon (BMC, black). b) Schematic of the mass and heat transportation showing water was transferred from the bottom through the macroporous geopolymer and then to the BMC layer heated by the solar energy. The effect can be enhanced by the negative pressure caused by wind. The water vapor finally released to the atmosphere and collected as the clean water. c) Schematic illustrations of materials synthesis and fabrication processes of the GBMCC solar steam generation devices.

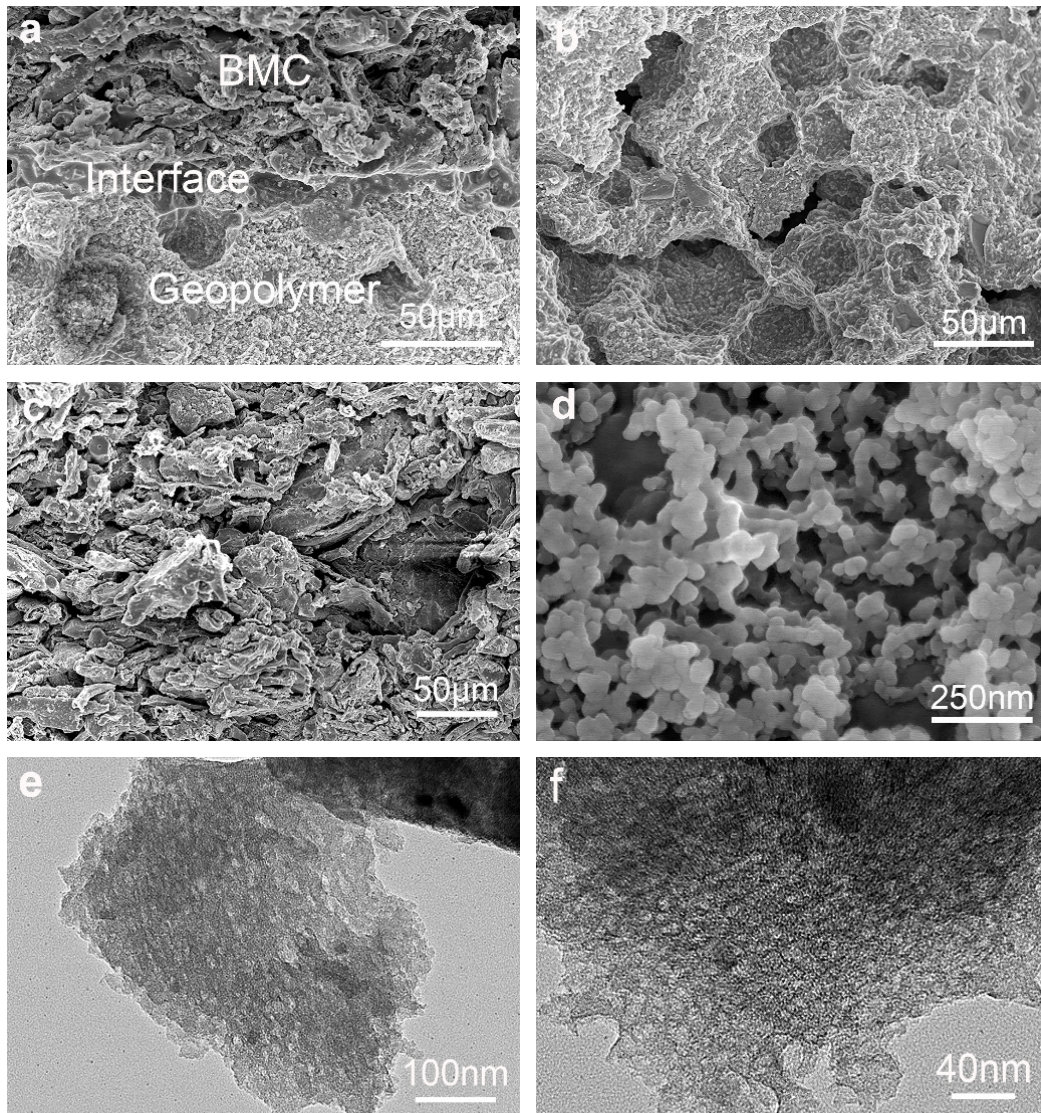


**Figure 2.** Typical morphology of the materials used for the GBMCC devices. a) The interface between the BMC and the geopolymer. The top layer is BMC, the bottom layer is geopolymer, the interfaces are internally very well connected as ideal barrierless water paths. b) Geopolymer with macro porous structures acting as channels for water transportation. c, d) High surface area BMCs with mesoporous intercommunicating mesh-like structures. e, f) TEM images of BMCs showing the materials consist of interconnected pores with diameters around 3 nm to 5 nm.

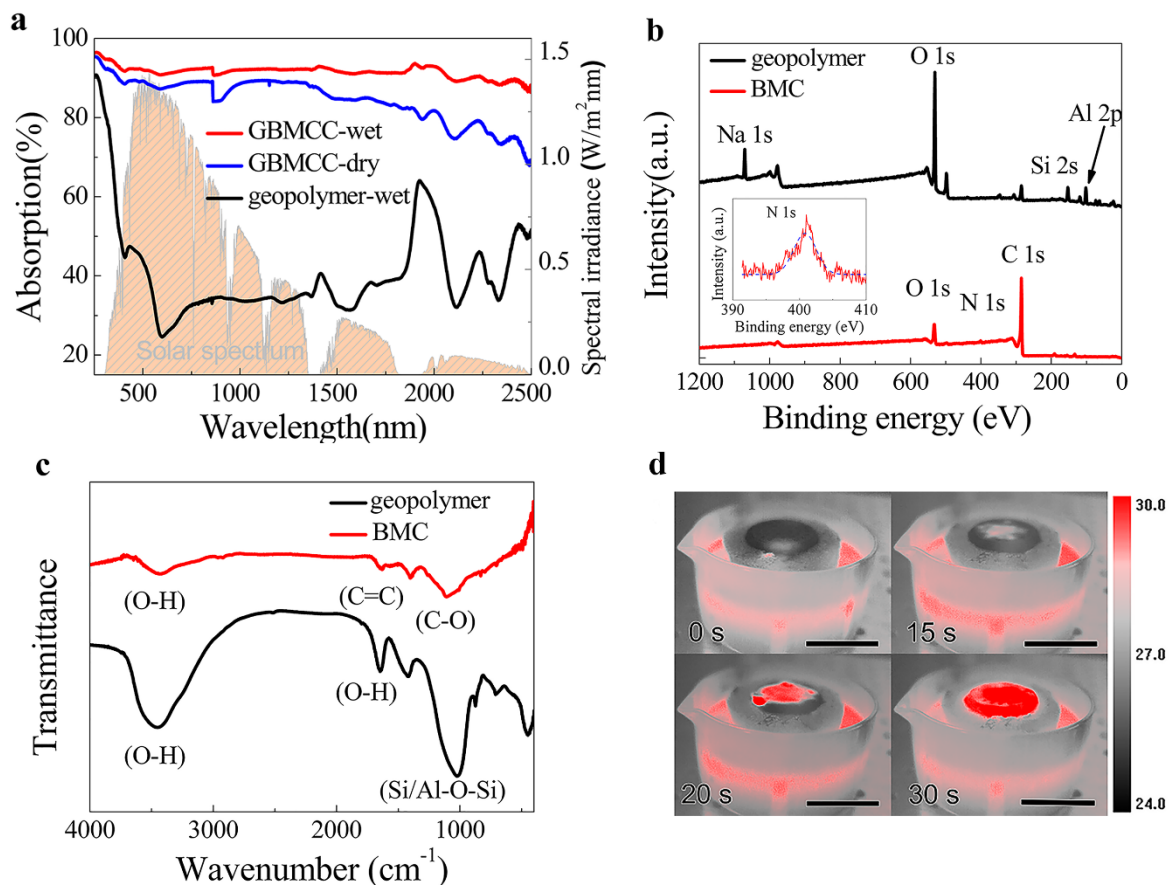


**Figure 3.** a) Solar spectral irradiance (AM 1.5 G) (gray, right hand side axis) and absorption (black, left hand side axis) of GBMCC(wet), GBMCC(dry), geopolymer (wet) samples. b) X-ray photoelectron spectroscopy (XPS) of geopolymer and BMC, inset shows the N 1S peak. c) FTIR spectra of geopolymer and BMC. d) Infrared photos of the wetting process of GBMCC device. The photos from top left to bottom right are corresponding to  $t = 0, 15, 20,$  and  $30$  s after the device is in touch with the water. Scale bar: 30 mm.

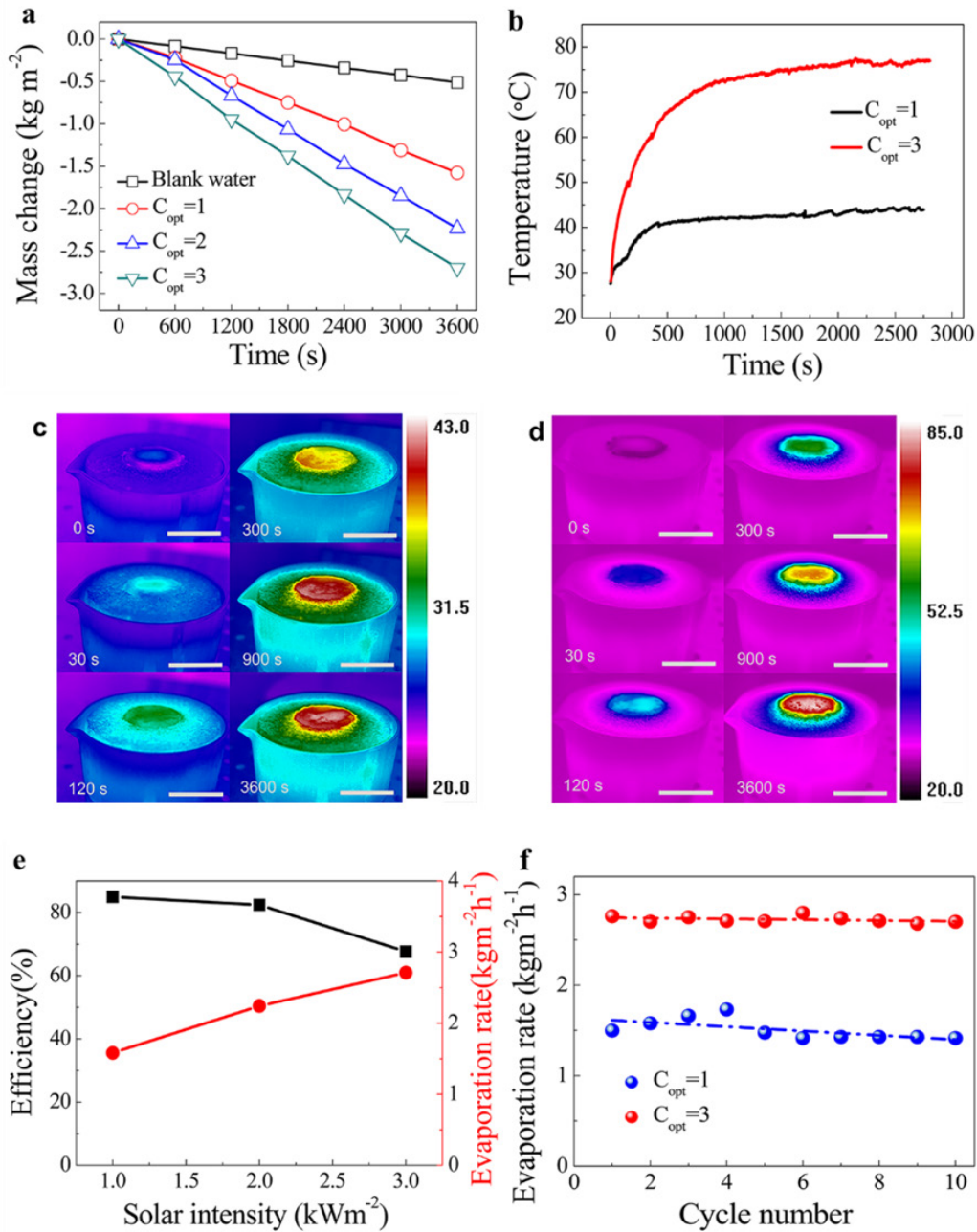


**Figure 4.** The steam generation performances of GBMCC devices under different solar illuminations. a) The water mass change over time under 1, 2 and 3 suns illumination. b) The average temperatures of surfaces for GBMCC as a function of time. The black and red lines both show the turning points to the quasi-steady state of GBMCC under 1 sun and 3 suns. c, d) Infrared imagines of the GBMCC surfaces under 1 sun and 3 suns, respectively. The imagines from top left to bottom right are corresponding to 0, 30, 120, 300, 900, and 3600 s after illumination. Scale bar: 30 mm. e) The efficiency and evaporation rate of the device under different illuminations. f) The cycle performance under 1 sun and 3 suns, respectively.

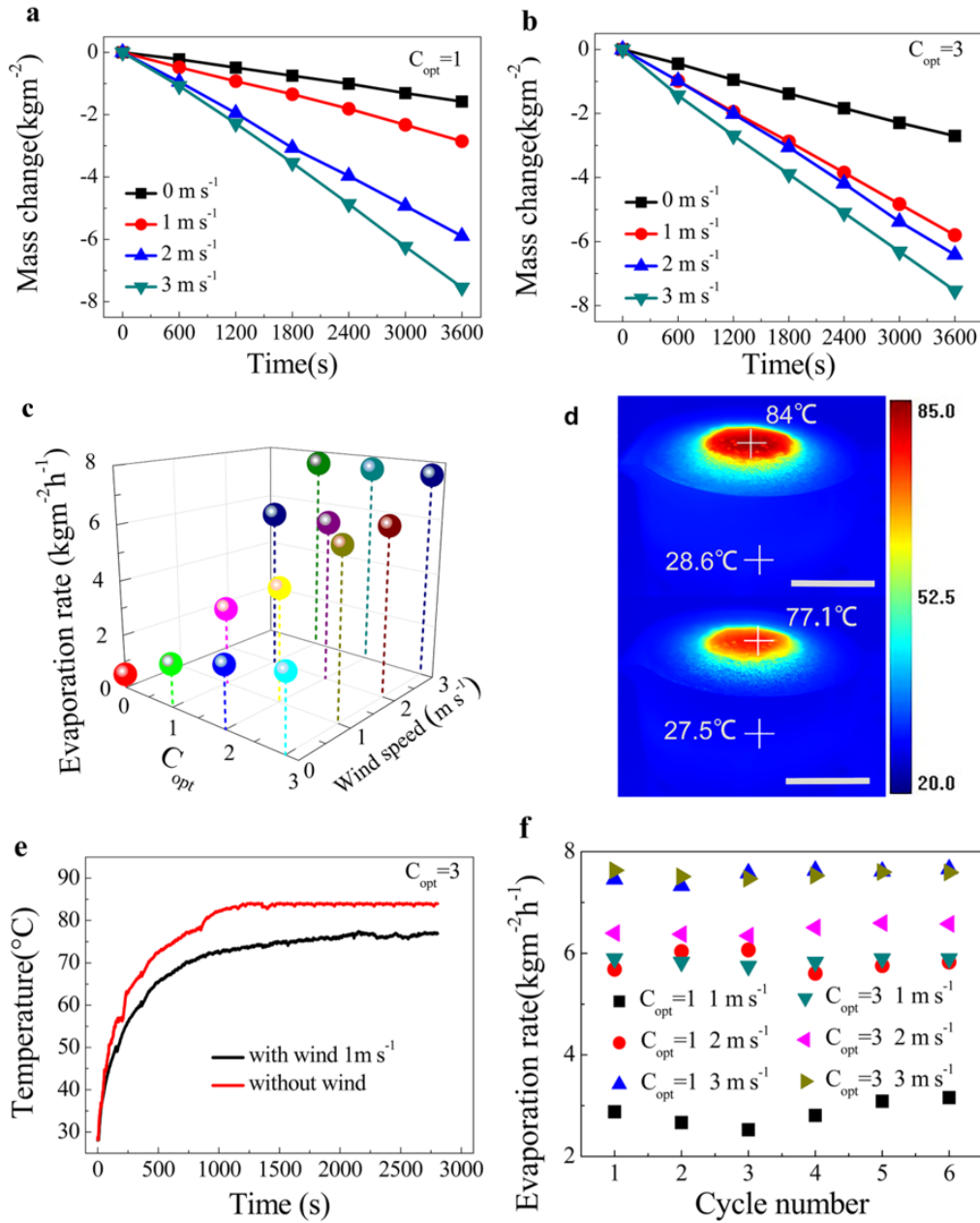


**Figure 5.** The solar steam generation performances of GBMCC devices upon wind flows. a, b) Water mass change at different wind speeds over time under 1 and 3 suns illumination, respectively. c) The influence of sunlight intensity and wind speed on evaporation rate. d) The infrared photos of the GBMCC surface at stable stage, and the top and bottom pictures are the photos of the surface temperature without and with wind (1 m s<sup>-1</sup>) under 3 suns, respectively. Scale bar: 30 mm. e) Maximum temperatures of surfaces for GBMCC with wind (1 m s<sup>-1</sup>) and without wind as a function of time under 3 suns. f) Cycle solar steam generation performance of the GBMCC under 1 and 3 suns.

# Supporting Information

## **Low Cost, Robust, Environmentally Friendly Geopolymer-Mesoporous Carbon Composites for Efficient Solar Powered Steam Generation**

*Fenghua Liu, Binyuan Zhao\*, Weiping Wu\*, Haiyan Yang, Yuesheng Ning, Yijian Lai and Robert Bradley*

Dr F. Liu, Prof. B. Zhao, Dr. H. Yang, Y. Ning, Y. Lai  
State Key Laboratory of Metal Matrix Composites,  
School of Materials Science and Engineering,  
Shanghai Jiao Tong University,  
Shanghai, 200240, China  
Email: byzhao@sjtu.edu.cn

Dr. W. Wu  
Department of Electrical and Electronic Engineering,  
School of Mathematics, Computer Science and Engineering,  
City, University of London  
Northampton Square, London, EC1V 0HB, United Kingdom  
Email: Weiping.Wu@city.ac.uk

Prof. R. Bradley  
Department of Materials, University of Oxford,  
16 Parks Road, Oxford,  
OX1 3PH, United Kingdom  
MatSurf Technology Ltd.  
The Old Stables Marion Lodge, Little Salkeld, Penrith,  
Cumbria, CA10 1NW, United Kingdom

### **Content:**

1. The preparation of the BMC
2. The mechanical properties of the BMC
3. The cost and environmental safety of the GBMCC devices
4. The pore structure and size distribution of the geopolymer
5. The nitrogen sorption isotherms and pore size distribution of the BMC
6. The solar reflectance of devices
7. The thermal conductivity calculation
8. The evaporation rate of water in dark environment and under 1 sun
9. The effect of geopolymer on water evaporation rate

## 1. The preparation of the BMC

Biomass mesoporous carbon (BMC) samples were prepared from corn straw. The compositional and structural information of BMCs are similar to those described in our previous work<sup>[1-3]</sup>. In brief, corn straw powder (20 g) was placed in a 100 mL beaker, then the mixture of phosphoric acid aqueous solution (10 mL, 30 wt%) and saturated aqueous oxalic acid solution (10 mL) was slowly added to the straw powder and stirred at 800 rpm for 15 min. KOH aqueous solution (8 mL, 5 wt%) was added in the above mixture and stirred for another 15 min. After being dried at 60 °C for 24 h, the powders was loaded into a mold for pressing (40 MPa) to get a bulk material. The bulk material was sintered at 800 °C in vacuum for 30 min, then the samples were cooled down to room temperature.

## 2. The mechinecal properties of the BMC

We carried out the compressive strength test and the bending strength test to evaluate the mechanical properties of BMC. The compressive strength test was performed with a universal testing machine (SANS CMT5105). The sample size was 47×47×18 mm and the constant load rate was 0.5 mm/min. The compressive strength of the BMC is about 35 MPa.

The bending strength was carried out with a Zwick Z020 universal testing machine. The test strip used for the test was 2×5×40 mm. It was measured by a three-point bending method with a span of 30 mm and a loading rate of 1 mm/min. The bending strength of the BMC is about 14 MPa.

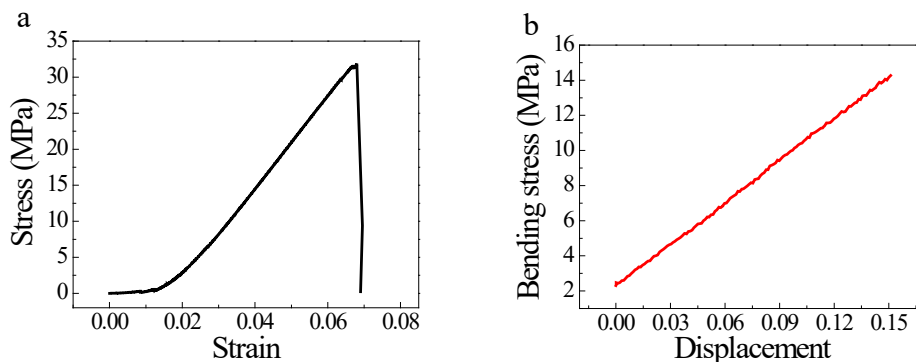


**Figure S1.** a) Compressive stress-strain curve of a BMC sample, b) Bending stress-displacement curve of a BMC sample.

### 3. The cost and environmental safety of the GBMCC devices

#### Cost estimation of the GBMCC devices

The GBMCC device comprises a geopolymer body (3.62 g) and a thin BMC absorber (1.8 g). The geopolymer slurry was made from low cost geopolymer powder (150 g, \$0.22/kg), DI water (55 mL) and hydrogen peroxide (2 g, 30 wt%). 5 g slurry (about 5/207 of the prepared slurry) can be made into the geopolymer body of a GBMCC device. The cost of the geopolymer is about \$0.22 per kg, which is close to the price data in Abdollahnejad and McLellan's previous work (<\$180 per ton).<sup>[4, 5]</sup>

The cost of the raw materials showed in the **Table S1**. The cost of the device is very low, as our carbon materials cost only about \$0.0147 per gram, much cheaper than the GO (\$26.5 per gram), Ti<sub>2</sub>O<sub>3</sub> (\$4.65 per gram) or other nano materials (Supplementary Section 3). The cost of one GBMCC device (3.62 g Geopolymer, 1.8 g BMC) is only \$0.0273. The estimated large area GBMCC devices cost \$39 per square meter only (\$39/m<sup>2</sup>).

**Table S1.** Cost of the materials for GBMCC device

	<b>H<sub>2</sub>O<sub>2</sub></b>	<b>Water</b>	<b>Geopolymer</b>	<b>BMC (raw materials, energy, labor)</b>	<b>Total</b>
<b>Unit cost (\$/kg)</b>	0.98	0.001	0.22	14.7	
<b>Weight (g)</b>	0.048	1.32	3.62	1.8	
<b>Cost</b>	0.00004704	0.00000132	0.0007964	0.02646	<b>0.0273</b>

#### Environmental safety of the GBMCC devices

Geopolymer is considered as the third-generation cement after lime and ordinary Portland cement.<sup>[6]</sup> A variety of aluminosilicate materials such as kaolinite, feldspar and industrial solid residues such as fly ash, blast furnace slag, mine tailings etc. have been used as solid raw materials<sup>[7-9]</sup> in the geopolymerization technology. The formation of geopolymer can occur under mild conditions with much lower CO<sub>2</sub> emission, lower energy consumption and thereby

is considered as a clean process<sup>[10]</sup>. It also has good durability which includes the resistance to chloride, acid, thermal, freeze-thaw and efflorescence. It also have the characters such as fire resistant (up to 1000 °C) and no emission of toxic fumes when heated,<sup>[11]</sup> antibacterial,<sup>[12]</sup> high level of resistance to a range of different acids and salt solutions, controlled delivery,<sup>[13]</sup> not subject to deleterious alkali-aggregate reactions.<sup>[14]</sup>

Elemental carbon has been used as an important and very successful biomaterial. The material is non-toxic, it has been used as filters for clean water and high quality air production, and additives for cosmetics and toothpastes. Also, researches prove that these carbon materials are safe to wear, no adverse events such as allergies or skin irritation occurred.<sup>[15]</sup> There are already many FDA approved products with carbon fillers on the market.

BMC is a biomass porous carbon which is made from plant straw, which can be pressed to a bulk carbon (size: 50×50×18mm). The material is non-toxic unlike many nano metal particles, reduced graphene oxide(rGO) powders or carbon nanotube. It is in the bulk form, dust free, it also has high specific surface area and developed porous structures. Due to the mechanical strength of GBMCC devices, they can be recycled easily. Therefore, they are environmentally friendly materials and devices.

#### 4. The pore structure and size distribution of the geopolymer

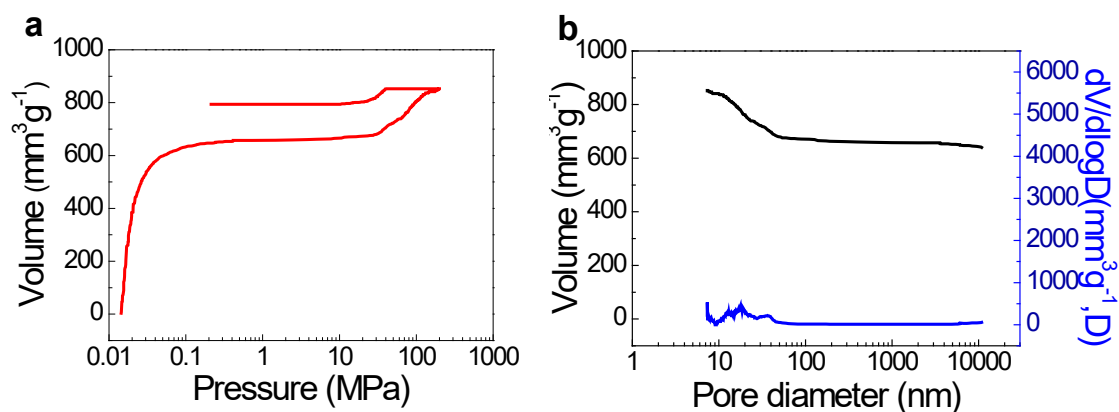


**Figure S2.** a) Volume of nitrogen adsorbed versus pressure curve of geopolymer, b) Pore size distribution curve of geopolymer.

5. The nitrogen sorption isotherms and pore size of the BMC

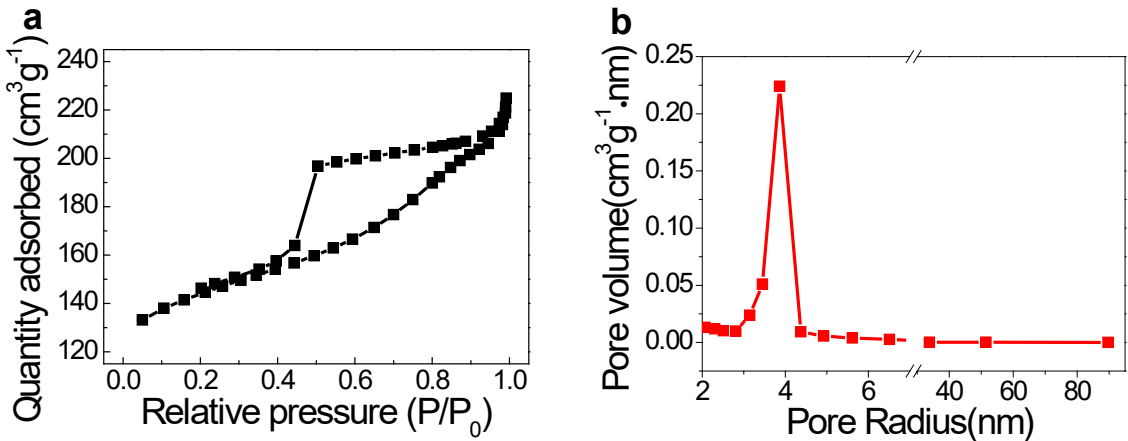


Figure S3. a) Nitrogen sorption isotherms, b) pore size distribution curve of BMC.

6. The solar reflectance of devices

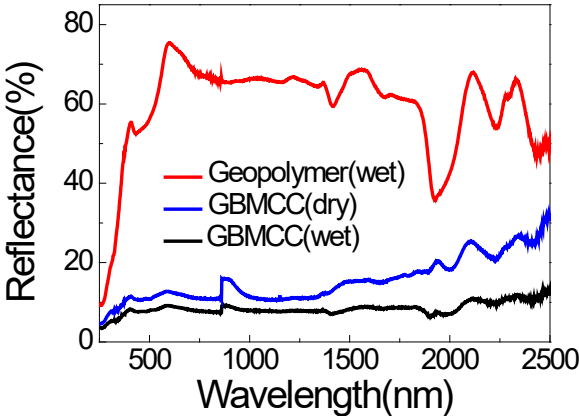


Figure S4. Solar reflectance of geopolymer (wet) shown as the red curve, GBMCC (dry) shown as the blue curve, GBMCC (wet) shown as the black curve. The reflectance of wet GBMCC is less about 8% over an ultra-broadband spectrum from 250 nm to 2500 nm.

## 7. The thermal conductivity calculation

The thermal conductivity of the geopolymer was calculated by experimental results. The Flash Method technique was used for the determination of thermal diffusivity on a Netzsch LFA 447 Nanoflash. The specific heat capacity was measured by differential scanning calorimetry (DSC 204 F1, Phoenix). The thermal conductivity of the geopolymer can be calculated with the formula (S1), which is showed below.

$$\alpha = \frac{\lambda}{\rho c} \quad (\text{S1})$$

where  $\alpha$  is thermal diffusion coefficient ( $0.369 \text{ mm}^2 \text{ s}^{-1}$ ),  $\lambda$  is heat conductivity,  $\rho$  is density of the material ( $2.36 \text{ g cm}^{-3}$ ) and  $c$  is specific heat ( $0.3 \text{ J g}^{-1} \text{ }^\circ\text{C}^{-1}$ ).

## 8. The evaporation rate of water in dark environment and under 1 sun

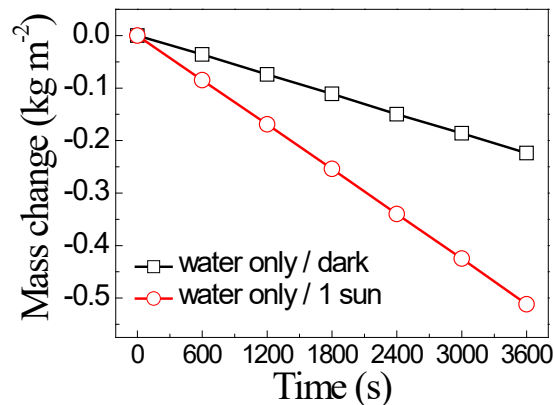


**Figure S5.** The evaporation rate in dark environment and under 1 sun.

## 9. The effect of geopolymer on water evaporation rate

According to the mass change plot of the the geopolymer without BMC layer under solar illumination (**Figure S6a**), we obtained that the value of  $0.72 \text{ kg m}^{-2} \text{ h}^{-1}$  ( $C_{opt}=1$ ),  $1.05 \text{ kg m}^{-2} \text{ h}^{-1}$  ( $C_{opt}=2$ ) and  $1.26 \text{ kg m}^{-2} \text{ h}^{-1}$  ( $C_{opt}=3$ ), respectively. In this experiment, only the top area which includes BMC and several hole instead by geopolymer is used to absorber the solar and wind energy, and the other parts are packaged by polyethylene foam. Based on the data

collected of geopolymer, we recalculated the water vapor data carefully which is excluded the influence of the geopolymer. The data details can be found in the **Table S2**.

$$m_{BMC} = \frac{m_{device} - m_{geopolymer}}{S_{BMC}} \quad (2)$$

$$m_{geopolymer} = v_{dgeopolymer} \times S_{geopolymer} \quad (3)$$

where  $m_{BMC}$ ,  $m_{device}$  and  $m_{geopolymer}$  are the mass loss rate per unit time calculated from the slop of mass loss curves at the steady state of BMC, device and geopolymer, respectively.  $S_{BMC}$  and  $S_{geopolymer}$  are the area in the device ( $S_{BMC}=7.701 \times 10^{-4} \text{ m}^2$ ,  $m_{geopolymer}=8.478 \times 10^{-5} \text{ m}^2$ ).  $v_{dgeopolymer}$  is the evaporation rate at the steady state. The mass change of the BMC without the effect of the geopolymer showed in **Figure S6b**.

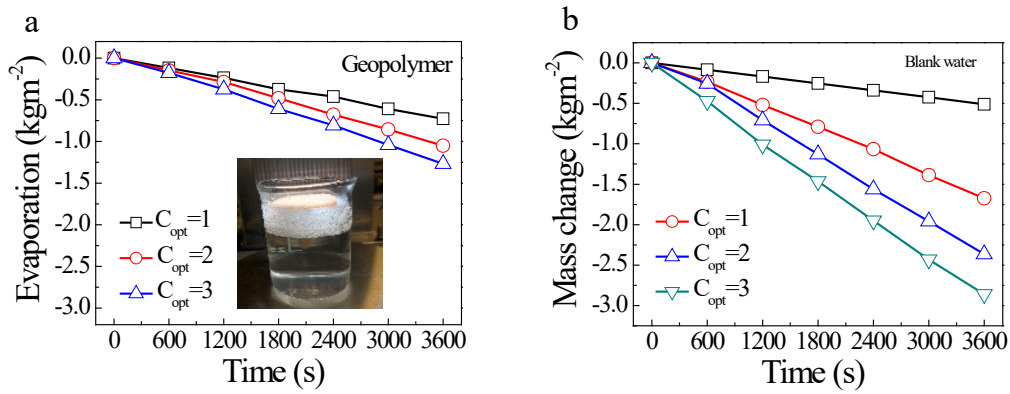


**Figure S6.** The mass change of the a) geopolymer and b) the device without the geopolymer influence.

**Table S2.** Mass change of the device without the effect of the geopolymer under different solar illumination.

Time /s	Mass change (kg m <sup>-2</sup> )			
	Blank water	$C_{opt}=1$	$C_{opt}=2$	$C_{opt}=3$
0	0	0	0	0
600	-0.085	-0.234	-0.256	-0.474
1200	-0.169	-0.519	-0.709	-1.011
1800	-0.254	-0.790	-1.129	-1.465
2400	-0.340	-1.066	-1.562	-1.950
3000	-0.425	-1.387	-1.958	-2.430
3600	-0.512	-1.673	-2.364	-2.860

## References

- [1] H. Zhao, Y. Ning, B. Zhao, F. Yin, C. Du, F. Wang, Y. Lai, J. Zheng, S. Li, L. Chen, *Sci. Rep.* **2015**, *5*, 13587.
- [2] J. Zhou, B. Y. Zhao, Q. Gan, R. B. Wang, Y. J. Lai, D. Zhang, K. A. Hu, *J. Mater. Sci.* **2007**, *42*, 6735.
- [3] F. Wang, Y. Lai, B. Zhao, X. Hu, D. Zhang, K. Hu, *Chem. Commun. (Cambridge, U. K.)* **2010**, *46*, 3782.
- [4] Z. Abdollahnejad, F. Pacheco-Torgal, T. Félix, W. Tahri, J. Barroso Aguiar, *Constr. Build. Mater.* **2015**, *80*, 18.
- [5] B. C. McLellan, R. P. Williams, J. Lay, A. van Riessen, G. D. Corder, *J. Cleaner Prod.* **2011**, *19*, 1080.
- [6] B. Singh, G. Ishwarya, M. Gupta, S. K. Bhattacharyya, *Constr. Build. Mater.* **2015**, *85*, 78.
- [7] Z. Abdollahnejad, F. Pacheco-Torgal, T. Félix, W. Tahri, J. Barroso Aguiar, *Constr. Build. Mater.* **2015**, *80*, 18.
- [8] I. García-Lodeiro, A. Palomo, A. Fernández-Jiménez, *Cem. Concr. Res.* **2007**, *37*, 175
- [9] C. Y. Heah, H. Kamarudin, A. M. Mustafa Al Bakri, M. Bnhussain, M. Luqman, I. Khairul Nizar, C. M. Ruzaidi, Y. M. Liew, *Constr. Build. Mater.* **2012**, *35*, 912.
- [10] D. Khale, R. Chaudhary, *J. Mater. Sci.* **2007**, *42*, 729.
- [11] J. Temuujin, W. Rickard, M. Lee, A. van Riessen, *J. Non-Cryst. Solids* **2011**, *357*, 1399.
- [12] M. Catauro, F. Bollino, F. Papale, G. Lamanna, *Mater. Sci. Eng., C* **2014**, *36*, 20.
- [13] E. Jamstorp, M. Stromme, G. Frenning, *J. Pharm. Sci.* **2011**, *100*, 4338.
- [14] I. García-Lodeiro, A. Palomo, A. Fernández-Jiménez, *Cem. Concr. Res.* **2007**, *37*, 175.
- [15] H. S. Scheer, M. Kaiser, U. Zingg, *J. Wound Care* **2017**, *26*, 476.